The Astrophysical Journal Letters, 933:L38 (7pp), 2022 July 10 https://doi.org/10.3847/2041-8213/ac7c73
© 2022. The Author(s). Published by the American Astronomical Society.
OPEN ACCESS

Are the Magnetic Field Directions of Surrounding Loops a Key Parameter for Confining a Solar Filament Eruption?

Tao Ding[1], Jun Zhang[1], and Junchao Hong[2]
[1] School of Physics and Optoelectronics Engineering, Anhui University, Hefei 230601, People's Republic of China; zjun@ahu.edu.cn
[2] Yunnan Observatories, Chinese Academy of Sciences, Kunming 650011, People's Republic of China
Received 2022 May 4; revised 2022 June 28; accepted 2022 June 28; published 2022 July 13

Abstract

Using high-resolution Hα data from the 1 m New Vacuum Solar Telescope, combined with multiband Atmospheric Imaging Assembly extreme ultraviolet observations and Helioseismic and Magnetic Imager light-of-sight magnetograms from the Solar Dynamical Observatory, we study a quiet-Sun filament eruption on 2019 November 1. During the erupting process, the filament was blocked by at least three sets of surrounding loops (L1–L3). The magnetic field direction of L2 is opposite to that of the top segment of the erupting filament. While the top segment contacted L2, a current sheet formed between L2 and the top segment. Then, magnetic reconnection took place, resulting in the destruction of L2 and the filament. On the other hand, the magnetic field direction of L1 is the same as that of the left leg of the erupting filament, and that of L3 is the same as that of the right leg. The left leg expanded eastward and met L1, then it stopped. The right leg expanded westward and collided with L3. It rebounded and finally stopped at the interaction region. These observations imply that the magnetic field directions of the surrounding magnetic structures are a key parameter for confining a filament eruption. While the field direction of a surrounding structure is the same as that of an eruptive filament, the filament is confined.

Unified Astronomy Thesaurus concepts: Solar activity (1475); Solar filaments (1495); Solar prominences (1519); Solar magnetic reconnection (1504); Solar magnetic fields (1503)

Supporting material: animations

1. Introduction

Solar filaments (or called prominences while they are appearing on or above the solar limb) are magnetic structures containing relatively dense (10^9–~10^{11}cm^{-3}) and cool (10^4 K) plasmas. They are normally suspended steadily in the corona above a photospheric magnetic polarity inversion line (PIL) or become unstable to erupt for some reason. Filament eruptions can be successful or not. Generally, a successful eruption is accompanied by a full coronal mass ejection (CME) process (Plunkett et al. 2000; Gopalswamy et al. 2003; Sterling & Moore 2004; Ma et al. 2010; Vourlidas et al. 2011).

However, filament eruptions are not always associated with CMEs. Ji et al. (2003) proposed the term failed eruption to define this special type of filament eruption without a CME. They reported that the erupting filament underwent a sharp deceleration after an initial eruptive-like acceleration. Then, the rising filament reached a maximum height, and its material drained back to the Sun. It is believed that the interaction between the filament and its associated magnetic environment results in the failed eruption (Williams et al. 2005; Török & Kliem 2005). Surrounding loops can hinder or change the kinetic evolution of erupting filaments (Zheng et al. 2017; Yang et al. 2018). Besides, magnetic reconnection between the filament-carrying magnetic field (Török et al. 2011) and surrounding loops will reconfigure or destroy the filament's main body (Amari & Luciani 1999; Yan et al. 2020; Yang et al. 2020). Zhou et al. (2019) found a complex coupling relationship between writhing and confined (failed) eruptions, and Hassanin & Kliem (2016) inferred that overlying constraints impel the erupting flux to relax the magnetic tension by writhing instead of expanding outward, indicating that this constraint could be an explanation for failed eruptions (Joshi et al. 2014). Moreover, an overlying field with a relatively large magnetic field strength would impose a strong confinement on an eruption. The decay index of the overlying magnetic field characterizes how quick the horizontal field strength decreases in altitude, and it is found that the overlying field, which decreases slowly with height, is an important factor resulting in eruption confinement (Török et al. 2004; Kliem & Török 2006; Chen et al. 2015). A laboratory experiment suggested that the magnetic tension force produced by the toroidal flux of the rope can confine the flux rope from erupting if such magnetic tension is strong enough (Myers et al. 2015). Liu et al. (2009) revealed that the asymmetric surrounding fields provide a stronger constraint on filament eruptions than symmetric fields do. Recently, the relationship between large solar flares and magnetic field parameters of active regions was investigated (Li et al. 2020, 2021). They suggested that magnetic flux and magnetic nonpotentiality are related to confined eruptions. Moreover, complex surrounding fields increase the possibility of erupting filaments being trapped in the low corona.

In this Letter, we study a detailed process of multiple surrounding loops confining a quiet-Sun filament eruption using high-resolution Hα observations from the 1 m New Vacuum Solar Telescope (NVST; Liu et al. 2014), as well as EUV images and magnetograms from the Solar Dynamic Observatory (SDO; Pesnell et al. 2012). In projection against the solar disk, the filament deforms from a smooth arc structure to several flattening segments while contacting these loops. Various activities at different segments take place, such as thread overflow, magnetic reconnection, to-and-fro motion, etc. Previous observations and simulation studies on confined eruptions commonly emphasize the restrictive role of the overlying field in some aspects, e.g., the

Original content from this work may be used under the terms of the Creative Commons Attribution 4.0 licence. Any further distribution of this work must maintain attribution to the author(s) and the title of the work, journal citation and DOI.

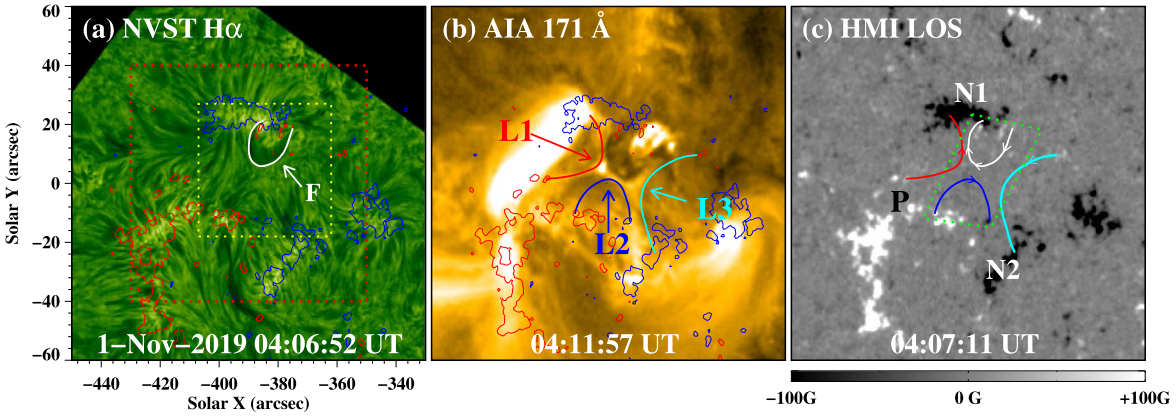

Figure 1. Overview of the erupting filament "F" in the NVST Hα image (panel (a)) and EUV loops "L1"–"L3" in SDO/AIA 171 Å image (panel (b)). The red square in panel (a) outlines the FOV in Figures 2 and 4(a1) and (b1), and the yellow square the FOV in Figures 3 and 5. The red and blue curves in panels (a)–(b) are contours of the SDO/HMI LOS magnetogram (panel (c)) at +30 G and −30 G, respectively. "P," "N1," and "N2" in panel (c) represent three magnetic patches in which the footpoints of the filament and the loops are rooted. Magnetic field directions relevant to the filament and the loops are denoted by corresponding arrows on the curves, and the green quadrilateral outlines the projection area in which the filament eruption is involved (panel (c)).

magnetic field strength and the decay index of the overlying flux. The data employed in this work provide a new chance to reveal whether one or all of these loops confine the filament eruption, and what parameter of the confining loop plays a key role.

2. Observations and Data Analysis

Around 03:30-04:30 UT on 2019 November 1, the NVST captured a small-scale filament eruption. The NVST data are taken in the Hα 6562.8 Å line, and the Hα images have a field of view (FOV) of 184″ × 188″ with a spatial resolution of 0.″165 and a time cadence of 11 s. To comprehend coronal responses of the eruption, we use multiwavelength EUV observations from the SDO/Atmospheric Imaging Assembly (AIA; Lemen et al. 2012) with a spatial resolution of 0.″6 and a time cadence of 12 s. Moreover, we apply SDO/Helioseismic and Magnetic Imager (HMI; Schou et al. 2012) light-of-sight (LOS) magnetograms, with a pixel size of 0.″5 and a cadence of 45 s, to determine the magnetic field directions of the filament and the surrounding loops. The AIA and HMI data are rotated differentially to a reference time (03:20:19 UT on 2019 November 1). Then, SDO and NVST images are coaligned by the cross-correlation method with specific features, e.g., structures "FS1" and "FS2," a bright point "BP," and an intersection "P1," which are detected by both Hα and AIA EUV observations (see Figures 2(a) and (c)).

The filament with an initial length of about 11 Mm is situated in the east of the solar disk (N01″, E25″). Around 03:50 UT the filament was activated then began to ascend and expand. After a slow-rising phase of 15 minutes, the expansion of the filament's left leg was first blocked by the eastern surrounding loop "L1" (Figures 1(a) and (b)). About 4 minutes later, the top segment of the filament started to come in contact with the southern loop "L2" (Figure 1(b)), and its southward expansion speed slowed down. Moreover, the filament's right leg continued to expand westward before 04:14 UT. Then, the right leg collided with loop L3 (Figure 1(b)) and stopped expanding. The main axis of the erupting filament "F" and the surrounding loops ("L1"–"L3") are superimposed on a magnetogram (Figure 1(c)).

Due to the constraints of L1 and L2, the left leg and the top segment of the filament gradually deformed and became flat ("FS1" and "FS2") at 04:09:26 and 04:11:06 UT, respectively. FS1, FS2, and their intersection ("P1") form an obtuse angle instead of a smooth arc structure as usual (Figure 2(a)). Similarly, the right leg deformed into two flattening structures ("FS3" and "FS4") because of the obstruction by L3 (Figure 2(b)). "P2" and "P3" are the intersections between FS2 and FS3, and between FS2 and FS3, respectively. In AIA EUV channels, FS1, FS2, and P1 are exhibited in composite of 171, 193 and 211 Å images (Figure 2(c)). An X-type structure with a sheet-like structure is displayed in Figure 2(d), and this sheet-like structure is essentially a current sheet.

During the process where the filament ascends and approaches L2, the top segment of the filament deformed to a flattening structure "FS2," then FS2 stopped expanding (Figures 3(a1)–(a3)). The HMI magnetogram (see also Figure 1(c)) implies that the magnetic field direction of FS2 is opposite to that of L2 at the interaction region. Therefore, the sheet-like structure shown in Figure 2(d) is plausibly a current sheet stressed at the interface between FS2 and L2. Figures 3(b1)–(b4) present the development of the current sheet. In the 171 Å channel, we observed a weak brightening (see the green box in Figure 3(b1)) appearing at the top of the filament near 04:06 UT. The brightening lasted for around a minute, with the peak brightness increasing by about 15% (see the smaller panel in Figure 3(b1)). Then, the brightening point evolved into a bright current sheet between FS2 and L2. Around 04:11:09 UT, the current sheet began to be observed clearly, and it reached a length of 8.5 Mm (Figure 3(b2)). Meanwhile, two EUV brightenings were observed, one at either end of the current sheet. The first one (see red arrows in Figure 3(b2)) appeared in the east of the current sheet at 04:09:26 UT and lasted until 04:13:19 UT. Around 04:10:45 UT, the second one (see green arrows in Figure 3(b2)) appeared in the west and was weaker than the former, lasting for about four minutes. Moreover, several bright moving features were detected inside the current sheet. Subsequently, they propagated both along "A–B" and "C–D" (Figures 3(b3) and (b4)). Around 04:17:39 UT, the filament broke up at FS2, then transient fibrils "TF1" and "TF2" were formed (Figure 3(a4)). Finally, filament materials were observed to drain back to both footpoints of TF1 (see two cyan circles in Figure 3(a4)) from 04:18 to 04:30 UT where the brightenings appeared.

The filament's main body appears a dark structure in AIA Fe lines (94, 131, 171, 193, 211 and 335 Å). However, the current sheet between the filament and L2 displays bright features in the emission of these Fe lines. Therefore, the emission measure (EM) and temperature within the current sheet can be obtained

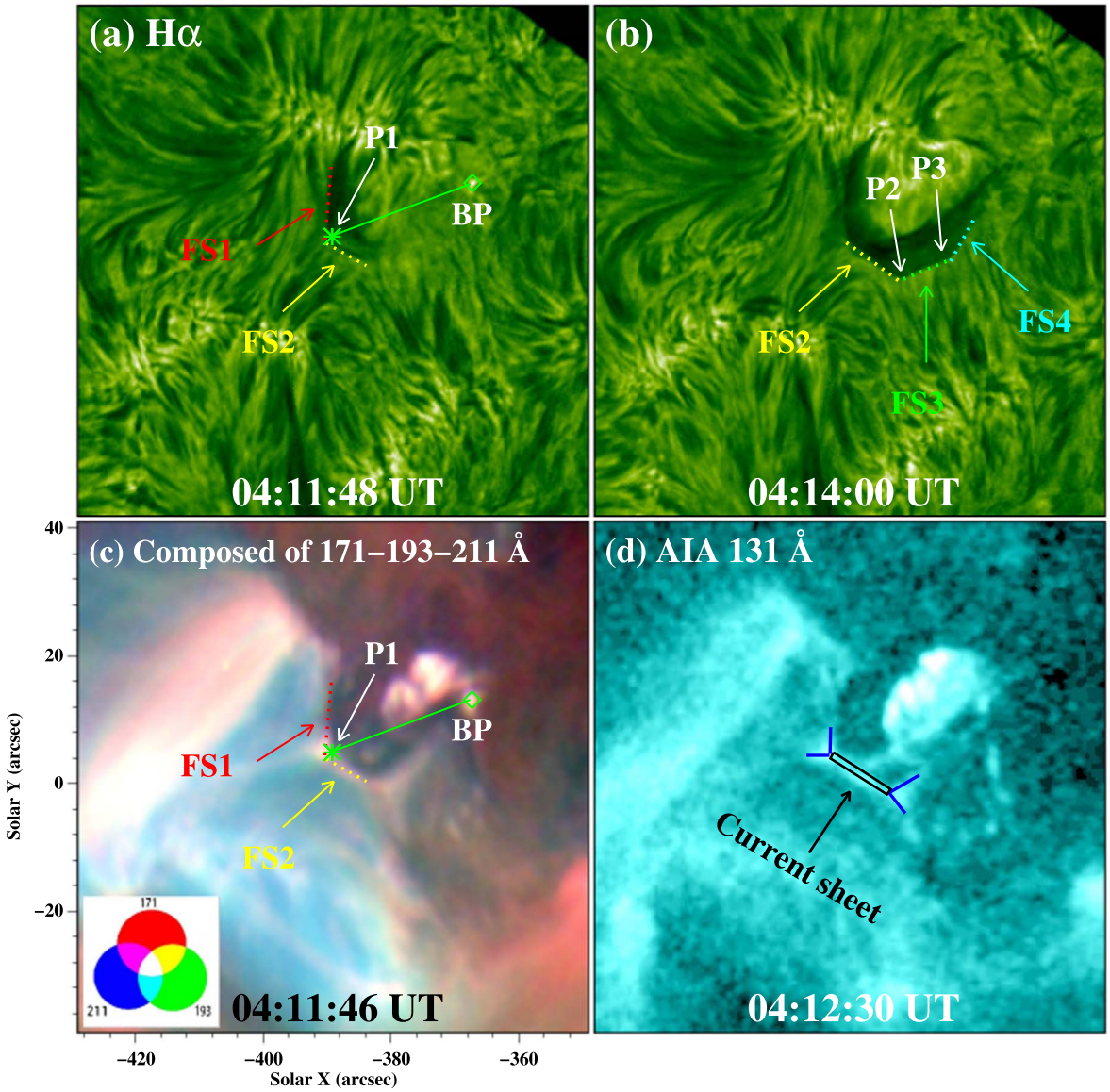

Figure 2. Images of Hα and multiband EUV displaying four flattening structures of the filament and an X-type structure with a current sheet. Panels (a) and (b): Hα observations showing the four flattening structures "FS1"–"FS4," which are underlined by red, yellow, green, and cyan dotted lines, respectively. "P1," "P2," and "P3" represent three intersections between FS1 and FS2, between FS2 and FS3, and between FS3 and FS4, separately. "BP" in panel (a) labels a bright point. Panel (c): composite of 171, 193, and 211 Å images exhibiting FS1, FS2, P1, and BP in AIA EUV channels. These specific features including "FS1," "FS2," "P1," and "BP" in panels (a) and (c) are used for the coalignment of NVST and SDO images. Panel (d): a 131Å image displaying the X-type structure with a current sheet.

with the almost simultaneous observations of the six AIA Fe lines via the differential emission measure (DEM) analysis (Plowman & Caspi 2020). The total EM and temperature can be calculated as $\mathrm{EM} = \int \mathrm{DEM}(T)dT$ and $T = \int \mathrm{DEM}(T)TdT/\mathrm{EM}$, respectively. In our calculation, the integral interval is selected as $5.5 \ll \mathrm{lgT} \ll 7.0$ to ensure the reliability of the results.

We further investigate the thermal evolution of plasmas in the current sheet. The first two rows in Figure 4 display the EM and temperature maps. During the interaction between the filament and L2, emission and temperature enhancements first appeared at the eastern end of the current sheet (see Figures 4(a1) and (b1)), e.g., in region "N" (Figures 4(a3) and (b3)) the EM and temperature reached $1.82 \times 10^{27}\mathrm{cm}^{-5}$ and 2.5 MK, respectively (Figure 4(e)). Inside the current sheet, they were also enhanced. For instance, the EM and temperature in region "M" marked in Figures 4(a2) and (b2) increased to $1.07 \times 10^{27}\mathrm{cm}^{-5}$ and 2.43 MK, separately (Figure 4(d)). The temperature evolution of regions "M" and "N" is displayed in Figure 4(c). Compared with region "N," the temperature in region "M" rises faster and reaches the peak earlier, but the peak temperature is lower.

According to the LOS magnetogram in Figure 1(c), we understand that both the eastern endpoint of the filament and the northern endpoint of L1 are rooted at the same negative magnetic patch "N1," which indicates that the magnetic field direction of the filament's left leg is the same as that of L1. From the time–distance plot made along "S2" (Figures 5(a1) and (b1)), it is easy to see that the left leg almost stopped its eastward expansion while it met L1. Subsequently, some dark thread-like structures could be observed at the left leg in Hα images (see Figures 5(a2) and (a3)). They underwent a "throwing whip" movement (an animation is attached), i.e., the tails of these threads swung clockwise. Checking the time–distance plot (Figure 5(b2)) along "S2" (see

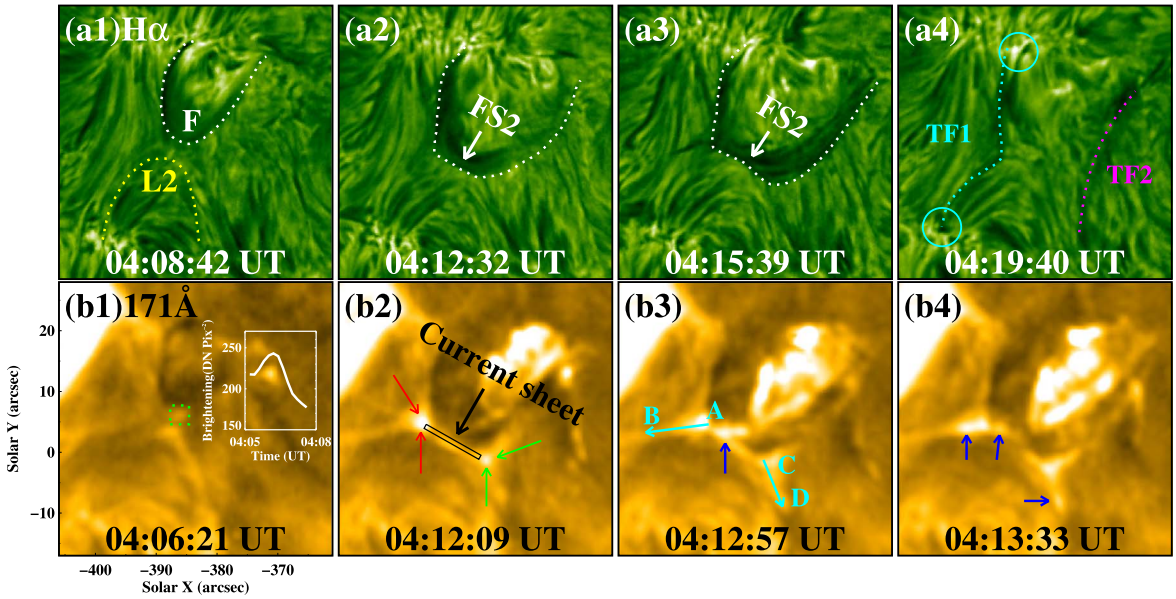

Figure 3. The interaction between FS2 and L2 observed in the Hα and 171 Å channels. The white, yellow, cyan, and purple dotted lines refer to the filament, the loop "L2", and the newly generated transient fibrils "TF1" and "TF2," respectively. Two cyan circles in panel (a4) display two footpoints of TF1. The smaller panel in panel (b1) represents the brightening variety of the 171 Å channel in the green box from 04:05:22 to 04:07:46 UT. The red and green arrows in panel (b2) denote two EUV brightenings, and the black rectangle marks the position of the current sheet. The blue arrows in panels (b3)–(b4) show the bright features. To display the evolution of the current sheet, an animation of the 171 Å observations is available, covering a duration from 04:05 to 04:21 UT.

(An animation of this figure is available.)

Figure 5(a2)), we find that at least five threads with lengths of 3–7 Mm were detected in Hα observations. These threads moved northward along S2 with speeds of about 24–33 km s^{-1} and lasted for 6–7 minutes. Then, they became totally invisible around 04:17:06 UT.

Similarly, the magnetic field direction of L3 is the same as that of the filament's right leg (Figure 1(c)). To show the dynamic evolution of the right leg during its expansion, two time–distance plots are made along "S3" (Figure 5(a3)) and "S4" (Figure 5(a4)). Like the time–distance plot (along "S3") displayed in Figure 5(b3), this segment (corresponding to FS3 marked in Figure 2(b)) of the right leg approached L3 with an average speed of 24.5 km s^{-1} before 04:13:38 UT, then rebounded to the northeast with a velocity of 16.4 km s^{-1} for about a minute. From the time–distance plot (along "S4") of Figure 5(b4), it is clear that this segment (see FS4 in Figure 2(b)) of the right leg had a similar kinetic evolution to FS3. Both FS3 and FS4 (they belong to the right leg) underwent to-and-fro motions while colliding with L3. Finally, the expansion of the right leg almost stopped at the interaction region.

3. Discussion and Conclusions

In this Letter, we report a quiet-Sun filament eruption confined by multiple loops. While the filament meets these loops, the filament's main body is compressed into four flattening structures (FS1–FS4). Different segments display different evolution patterns. FS1 keeps connecting, with only several thread-like materials overflowing. Similarly, the right leg (FS3 and FS4) also maintains connection and undergoes a to-and-fro motion. The evolution of FS2 is relatively different from that of FS1, FS3, and FS4. At first, a current sheet appears between FS2 and L2. Then, magnetic reconnection takes place and FS2 breaks up. Eventually, the filament material drains along the legs of the filament and L2, and the filament becomes invisible. This eruption is thereby confined to a local region by surrounding loops, meaning that the eruption process does not disturb the large-scale background atmosphere and magnetic field.

The interaction between an erupting filament and another solar atmospheric structure is a common phenomenon. It can change the kinetic motion of erupting filaments. For example, an erupting filament collided with a coronal hole directly, resulting in the filament being bounced off and shrinking of the coronal hole (Jiang et al. 2007), and an ascending filament was deflected nearly 90° by open magnetic fields (Yang et al. 2018). Moreover, some observations showed that erupting filaments can be influenced and guided by surrounding loops (Panasenco et al. 2011; Kay et al. 2013; Zheng et al. 2017). In our event, the left and right legs of the filament are finally forced to stop at their interaction region by L1 and L3, respectively, with some threads overflowing at the left leg and a to-and-fro motion at the right leg.

Most reports revealed that when two sets of magnetic lines with opposite polarities approach each other, a current sheet appears between them, and magnetic reconnection occurs. As a result, the magnetic topology is changed and new magnetic connectivity is generated (Parker 1957; Sweet 1958; Petschek 1964; Vasyliunas 1975). In this event, many observational evidences support the idea that magnetic reconnection takes place between FS2 (one segment of the filament) and L2. First, the current sheet is definitely established between the opposite magnetic field of FS2 and L2. Second, EUV brightenings, bi-propagating bright features, and plasma heating are all detected around the current sheet. Finally, the filament disconnects inside the current sheet. These aspects match well with previous magnetic reconnection models and observations (Yokoyama et al. 2001; Drake et al. 2003; Kumar et al. 2010; Edmondson et al. 2010; Yang et al. 2015; Li et al. 2016).

While a filament eruption is relevant to a CME, the filament may go through internal and external reconnection. The internal reconnection accelerates the ascent of the filament, and the external reconnection destroys the upper magnetic

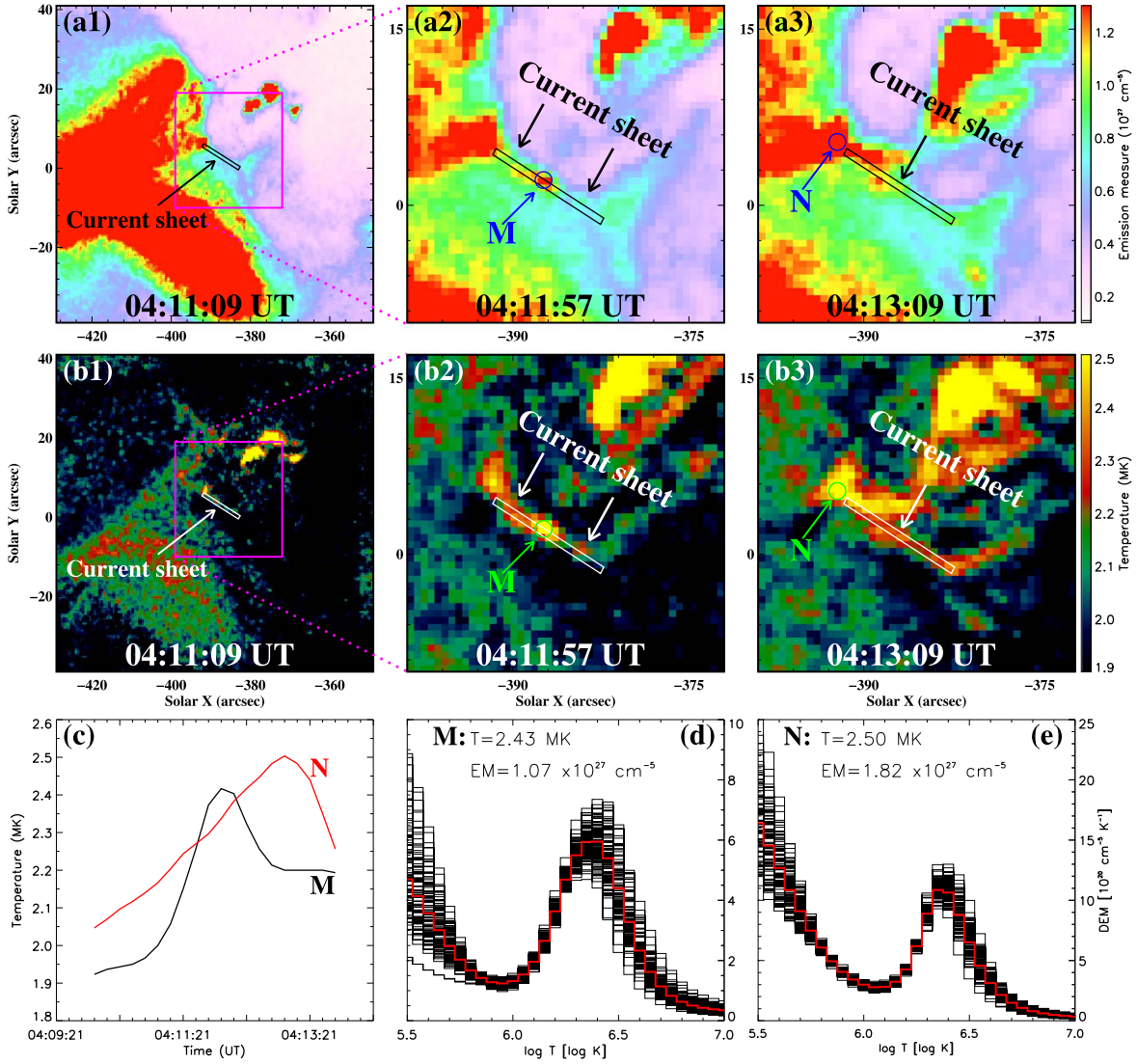

Figure 4. DEM results at the interaction region of FS2 and L2. The first two rows show the EM and temperature maps. Purple boxes in panels (a1) and (b1) outline the FOV of panels (a2), (a3), (b2), and (b3). The temperature curves of regions "M" (panels (a2) and (b2)) and "N" (panels (a3) and (b3)) are given in panel (c). Panels (d)–(e) display the averaged DEM distributions of regions "M" and "N," respectively. The red curves in panels (d)–(e) are the optimum DEM distributions while the black curves are the results of 100 Monte Carlo simulations, suggesting that the solutions are very reliable.

structure to make the core erupt successfully (Sterling & Moore 2004; Vourlidas et al. 2011; Green et al. 2018). As for confined eruptions, magnetic reconnection between a filament and a surrounding loop is not rare (Ji et al. 2003; Netzel et al. 2012; Kuridze et al. 2013; Mason et al. 2021; Peng et al. 2022). Yan et al. (2020) reported an observational case of an erupting filament being partially disconnected by the confining loop. Furthermore, the reconnection would lead to the disintegration of a filament and the launch of a jet (Yang et al. 2020). Although reconnection can weaken the constraint of the confining loop to facilitate the eruption (Liu & Su 2021), in some cases, the reconnection will play a negative role in magnetic flux rope eruption (Mason et al. 2021; Peng et al. 2022). Mason et al. (2021) suggested that a well-defined line that developed from the reconnection could restrict the expansion of a prominence as it reconnected and relaxed. Further, simulation has also revealed that the reconnection process results in a stronger confining field and thus leads to a failed eruption (Hassanin & Kliem 2016). In our observations, FS2 undergoes a thorough X-type magnetic reconnection process, and the filament seems to be disconnected completely. However, it is difficult to confirm the positive or negative role of magnetic reconnection in this eruption.

The reconnection changes the topology of magnetic structures. In this work, obvious magnetic reconnection between FS2 and L2 began around 04:11:09 UT. Besides, dark thread-like structures at FS1 appeared later than the reconnection (see Figure 5(b2)). Therefore, it is suggested that these threads may be segments of the newly formed loops generated by the reconnection between FS2 and L2. Moreover, the appearance of FS3 also followed the magnetic reconnection. Figures 2(b) and (d) display that FS3 coincides with a western part of the X-type structure. It is possible that the newly formed loops would modulate the filament structure and result in the deformation of FS3, which indicates that the change in the filament structure from a smooth arc shape to several flattening structures is probably caused by both preexisting and newly formed loops.

The drainage phenomenon, wherein the filament material drains back to the nearby disk after the filament reaches a certain height (Ji et al. 2003; Alexander et al. 2006;

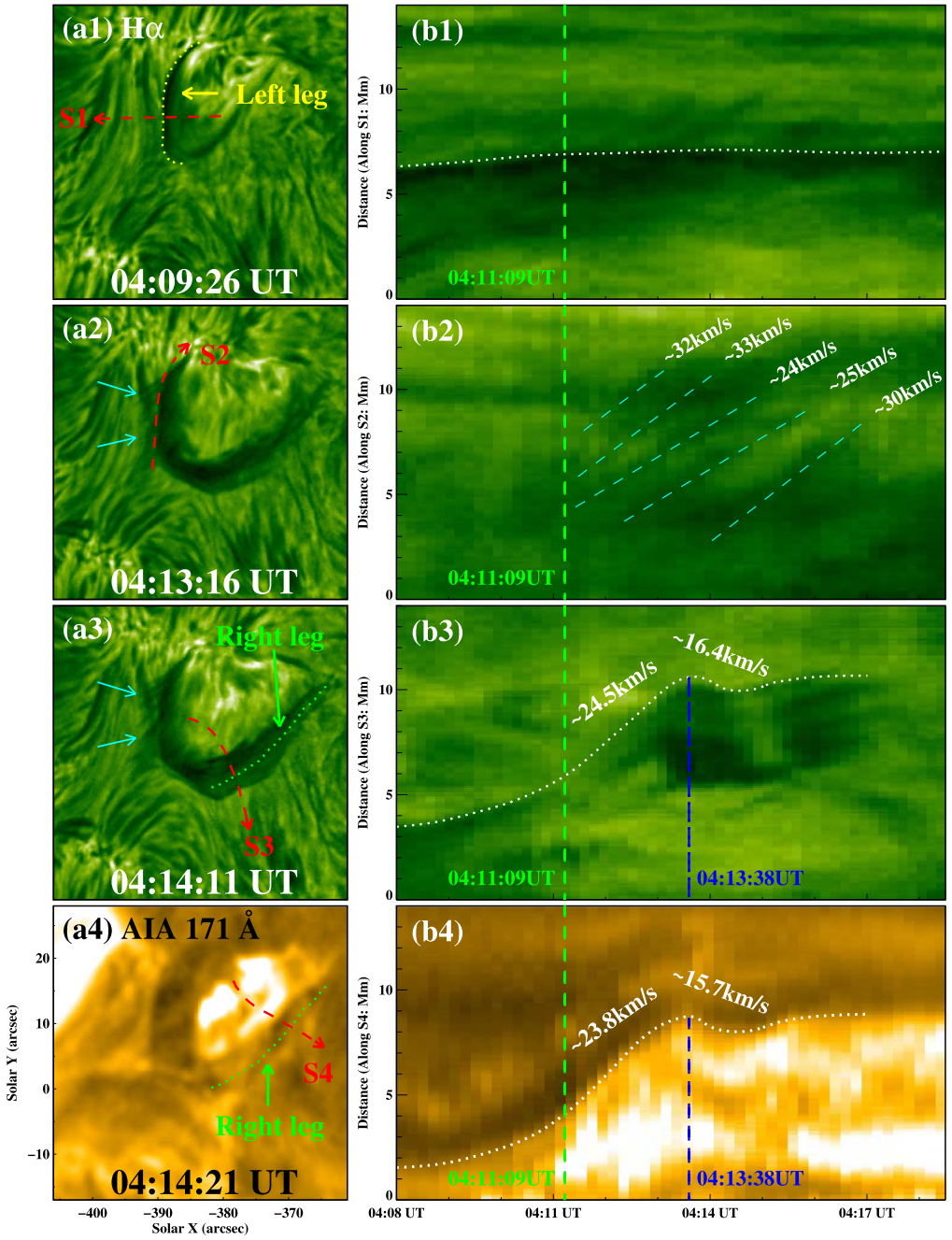

Figure 5. The dynamics of the filament's left and right legs. Left row: Hα (panels (a1)–(a3)) and AIA 171 Å (panel (a4)) images showing the erupting filament. The yellow dotted line in panel (a1) and the green dotted lines in panels (a3)–(a4) represent the filament's left and right legs, separately. Several thread-like structures are labeled by cyan arrows in panels (a2) and (a3). Panels (b1)–(b4) are the time–distance plots along "S1"–"S4" (see panels (a1)–(a4)), respectively. The green vertical lines (04:11:09 UT) in panels (b1)–(b4) indicate the start time of the obvious reconnection between FS2 and L2. The blue dashed lines (04:13:38 UT) in panels (b3) and (b4) denote the start time of the rebounding at the right leg. An animation of Hα observations from 04:05 to 04:26 UT, showing the thread overflowing at the left leg and the to-and-fro motion at the right leg, is available.

(An animation of this figure is available.)

McCauley et al. 2015), transfers into newly generated loops after the filament and a confining loop exchange connectivity (Yan et al. 2020), or moves back into the same stable magnetic structure and re-forms the filament (Joshi et al. 2014), has been widely reported. In this event, we observed the drainage of the filament material along the legs of the filament and L2; the filament then disappeared in situ. No observational evidence shows that the filament material escapes from the lower atmosphere to the upper corona, so the upper atmosphere structure is not disturbed or destroyed.

In order to estimate quantitatively the spatial scale involved in this event, we try to determine the projected area S and the largest height H of the confining loops. The quadrilateral in Figure 1(c) determined by four apexes represents the projected area S in which EUV brightening or filament material accumulation appears at the later phase of the filament eruption, and the largest height H is chosen as half of the distance of the two endpoints of L2. S is about 650 Mm^2 and H nearly 8.5 Mm, so the volume V is estimated to be 5500 Mm^3. To our knowledge, for an erupting filament that undergoes a

full reconnection process, the confined volume with such a small size has never been reported before.

Overall, despite a single to-and-fro motion at the right leg, both legs of the filament are almost halted at their interaction regions with surrounding loops (L1 and L3). Photospheric magnetic field observations indicate that the magnetic field directions of the left leg and L1 (the right leg and L3) are almost the same, suggesting that the magnetic field directions of the surrounding magnetic structures are a key parameter for confining a filament eruption. While the field direction of a surrounding structure is the same as that of an eruptive filament, the filament is confined. In this Letter, we have only displayed one event where surrounding loops with the same magnetic field directions as the erupting filament confine the filament eruption. To confirm this result, more cases with high-resolution observations are needed.

The authors thank the anonymous referee for constructive suggestions and helpful comments. The observations used in our work are provided by NVST and SDO teams. This work is supported by the National Natural Science Foundation of China (12073001, 11790300, and 11790304), the Anhui Project (Z010118169), and the open topic of the Key Laboratory of Solar Activities of the Chinese Academy of Sciences (KLSA202116).

ORCID iDs

Tao Ding https://orcid.org/0000-0002-5383-1129
Jun Zhang https://orcid.org/0000-0002-1286-6931
Junchao Hong https://orcid.org/0000-0002-3804-7395

References

Alexander, D., Liu, R., & Gilbert, H. R. 2006, ApJ, 653, 719
Amari, T., & Luciani, J. F. 1999, ApJL, 515, L81
Chen, H., Zhang, J., Ma, S., et al. 2015, ApJL, 808, L24
Drake, J. F., Swisdak, M., Cattell, C., et al. 2003, Sci, 299, 873
Edmondson, J. K., Antiochos, S. K., DeVore, C. R., Lynch, B. J., & Zurbuchen, T. H. 2010, ApJ, 714, 517
Gopalswamy, N., Shimojo, M., Lu, W., et al. 2003, ApJ, 586, 562
Green, L. M., Török, T., Vršnak, B., Manchester, W., & Veronig, A. 2018, SSRv, 214, 46
Hassanin, A., & Kliem, B. 2016, ApJ, 832, 106
Ji, H., Wang, H., Schmahl, E. J., Moon, Y. J., & Jiang, Y. 2003, ApJL, 595, L135
Jiang, Y., Yang, L., Li, K., & Shen, Y. 2007, ApJL, 667, L105
Joshi, N. C., Srivastava, A. K., Filippov, B., et al. 2014, ApJ, 787, 11
Kay, C., Opher, M., & Evans, R. M. 2013, ApJ, 775, 5
Kliem, B., & Török, T. 2006, PhRvL, 96, 255002
Kumar, P., Manoharan, P. K., & Uddin, W. 2010, ApJ, 710, 1195
Kuridze, D., Mathioudakis, M., Kowalski, A. F., et al. 2013, A&A, 552, A55
Lemen, J. R., Title, A. M., Akin, D. J., et al. 2012, SoPh, 275, 17
Li, L., Zhang, J., Peter, H., et al. 2016, NatPh, 12, 847
Li, T., Chen, A., Hou, Y., et al. 2021, ApJL, 917, L29
Li, T., Hou, Y., Yang, S., et al. 2020, ApJ, 900, 128
Liu, T., & Su, Y. 2021, ApJ, 915, 55
Liu, Y., Su, J., Xu, Z., et al. 2009, ApJL, 696, L70
Liu, Z., Xu, J., Gu, B.-Z., et al. 2014, RAA, 14, 705
Ma, S., Attrill, G. D. R., Golub, L., & Lin, J. 2010, ApJ, 722, 289
Mason, E. I., Antiochos, S. K., & Vourlidas, A. 2021, ApJL, 914, L8
McCauley, P. I., Su, Y. N., Schanche, N., et al. 2015, SoPh, 290, 1703
Myers, C. E., Yamada, M., Ji, H., et al. 2015, Natur, 528, 526
Netzel, A., Mrozek, T., Kołomański, S., & Gburek, S. 2012, A&A, 548, A89
Panasenco, O., Martin, S., Joshi, A. D., & Srivastava, N. 2011, JASTP, 73, 1129
Parker, E. N. 1957, JGR, 62, 509
Peng, Z., Chaowei, J., Juntao, W., & Xinkai, B. 2022, ApJ, 928, 160
Pesnell, W. D., Thompson, B. J., & Chamberlin, P. C. 2012, SoPh, 275, 3
Petschek, H. E. 1964, NASA Spec. Publ., The Physics of Solar Flares, Vol. 50 (Washington, DC: NASA, Science and Technical Information Division), 425
Plowman, J., & Caspi, A. 2020, ApJ, 905, 17
Plunkett, S. P., Vourlidas, A., Šimberová, S., et al. 2000, SoPh, 194, 371
Schou, J., Scherrer, P. H., Bush, R. I., et al. 2012, SoPh, 275, 229
Sterling, A. C., & Moore, R. L. 2004, ApJ, 613, 1221
Sweet, P. A. 1958, in IAU Symp. 6, Electromagnetic Phenomena in Cosmical Physics, ed. B. Lehnert (Cambridge: Cambridge Univ. Press), 123
Török, T., Chandra, R., Pariat, E., et al. 2011, ApJ, 728, 65
Török, T., & Kliem, B. 2005, ApJL, 630, L97
Török, T., Kliem, B., & Titov, V. S. 2004, A&A, 413, L27
Vasyliunas, V. M. 1975, RvGSP, 13, 303
Vourlidas, A., Colaninno, R., Nieves-Chinchilla, T., & Stenborg, G. 2011, ApJL, 733, L23
Williams, D. R., Török, T., Démoulin, P., van Driel-Gesztelyi, L., & Kliem, B. 2005, ApJL, 628, L163
Yan, X., Xue, Z., Cheng, X., et al. 2020, ApJ, 889, 106
Yang, J., Dai, J., Chen, H., Li, H., & Jiang, Y. 2018, ApJ, 862, 86
Yang, J., Hong, J., Li, H., & Jiang, Y. 2020, ApJ, 900, 158
Yang, S., Zhang, J., & Xiang, Y. 2015, ApJL, 798, L11
Yokoyama, T., Akita, K., Morimoto, T., Inoue, K., & Newmark, J. 2001, ApJL, 546, L69
Zheng, R., Zhang, Q., Chen, Y., et al. 2017, ApJ, 836, 160
Zhou, Z., Cheng, X., Zhang, J., et al. 2019, ApJL, 877, L28